Strong perpendicular anisotropic ferromagnet Fe<inf>3</inf>GeTe<inf>2</inf>/graphene van der Waals heterostructure

N.B. When citing this work, cite the original published paper.

(article starts on next page)

PAPER • OPEN ACCESS

Strong perpendicular anisotropic ferromagnet Fe$_3$GeTe$_2$/graphene van der Waals heterostructure

To cite this article: Bing Zhao *et al* 2023 *J. Phys. D: Appl. Phys.* **56** 094001

View the article online for updates and enhancements.

Strong perpendicular anisotropic ferromagnet Fe$_3$GeTe$_2$/graphene van der Waals heterostructure

Bing Zhao[1,4,*] , **Bogdan Karpiak**[1,4], **Anamul Md Hoque**[1] , **Pallavi Dhagat**[2] and **Saroj P Dash**[1,3,*]

[1] Quantum Device Physics Laboratory, Department of Microtechnology and Nanoscience, Chalmers University of Technology, SE-41296 Göteborg, Sweden

[2] School of Electrical Engineering and Computer Science, Oregon State University, Corvallis, OR 97331, United States of America

[3] Graphene Center, Chalmers University of Technology, SE-41296 Göteborg, Sweden

E-mail: zbing@chalmers.se and saroj.dash@chalmers.se

CrossMark

Abstract

Two-dimensional magnets offer a new platform for exploring fundamental properties in van der Waals (vdW) heterostructures and their device applications. Here, we investigated heterostructure devices of itinerant metallic vdW ferromagnet Fe$_3$GeTe$_2$ (FGT) with monolayer chemical vapor deposited graphene. The anomalous Hall effect measurements of FGT Hall-bar devices exhibit robust ferromagnetism with strong perpendicular anisotropy at low temperatures. The electrical transport properties measured in FGT/graphene heterostructure devices exhibit a tunneling transport with weak temperature dependence. We assessed the suitability of such FGT/graphene heterostructures for spin injection and detection and investigated the presence of FGT on possible spin absorption and spin relaxation in the graphene channel. These findings will be useful for engineering spintronic devices based on vdW heterostructures.

Keywords: Fe$_3$GeTe$_2$, graphene, van der Waals heterostructure, spin transport, spin absorption

(Some figures may appear in colour only in the online journal)

1. Introduction

Magnetic van der Waals (vdW) materials exhibit ordered magnetic properties in atomically thin two-dimensional (2D) layers [1–6]. Such a family of 2D magnets has been proliferating over the past few years with the unearthing of metallic [7, 8], insulating [9], and semiconducting crystals [10, 11]. The functionality of such vdW magnets is enormous because of the tunability of magnetic order parameters, such as the critical temperature, coercive field, and magnetic textures, which can be controlled by an electric field, strain, and proximity effects [12–15]. Recently, such vdW magnets were utilized to demonstrate various spintronic and quantum phenomena, such as giant tunneling magnetoresistance (MR), spin-valves, spin–orbit torque, magnon transport, skyrmions, and proximity-induced magnetic exchange and topological quantum states [1, 2, 16–18].

---

[4] These authors contributed equally.

[*] Authors to whom any correspondence should be addressed.

The assembly of vdW heterostructures by combining vdW magnets with other 2D materials can allow the development of new device concepts. Heterostructures of vdW magnets with semiconductors [19], topological insulators [20], semimetals [21], and graphene [18] have shown significant magnetic proximity effects and breaking of the time-reversal symmetry for the realization of novel spin textures. Specifically, vdW metallic ferromagnets Fe_xGeTe_2 with perpendicular magnetic anisotropy (PMA) are potential materials for making heterostructures with graphene for spin injection and detection, and investigation of spin absorption and proximity effects. Recently, room-temperature spin injection and detection have been observed in Fe_5GeTe_2/graphene heterostructures, revealing a canted magnetization [22]. On the other hand, Fe_3GeTe_2 (FGT) has emerged as one of the fascinating vdW crystals due to its strong PMA [23, 24], however, its heterostructure devices with graphene spin-valves remained unexplored.

Here, we present heterostructure devices of metallic itinerant vdW ferromagnet FGT with monolayer chemical vapor deposited (CVD) graphene. The magnetic properties of the FGT nanoflake Hall-bar devices were measured employing the anomalous Hall effect (AHE), exhibiting PMA with a strong dependence of coercivity on the angle between the out-of-plane axis and the direction of the applied magnetic field. In the FGT/graphene heterostructure, we evaluate the relevance of the vdW contacts for spin injection and spin absorption in graphene spintronic devices. These findings could be useful for engineering vdW heterostructure-based devices and spin logic circuits [25].

2. Results and discussions

2.1. Device fabrication and electrical measurements

We nanofabricated the FGT Hall-bars and FGT/graphene heterostructures spin-valve devices on Si/SiO_2 substrates. The FGT flakes were exfoliated from single crystal samples (from Hq Graphene) placed on patterned CVD graphene stripes on Si/SiO_2 substrate in a glove box in an N_2 environment. The schematic and optical microscope picture of a representative FGT/graphene heterostructure device is shown in figures 1(a) and (b). The nonmagnetic Ti/Au contacts on FGT and graphene and magnetic contacts TiO_2/Co on graphene were prepared using electron beam lithography and e-beam evaporation techniques. In order to get an Ohmic contact between the Ti/Au electrodes and the FGT, a mild Ar milling cleaning process was performed before the deposition of the Ti/Au contacts. The contact resistance between Ti/Au and the FGT is below tens of Ω, while the channel of FGT is $\sim$1 kOhm.

First, we present the characterization of only FGT flakes. The typical Raman spectrum of FGT with three prominent Raman modes at room temperature with $E_{2g}^1 = 102.7$ cm^{-1} and $A_{1g}^1 = 125.7$ cm^{-1}. Such peaks agree well with recent studies with different thickness and temperature effect which is free of strain, confirming the high quality of the crystal [26, 27]. The temperature dependence of resistance of an FGT flake of $\sim$30 nm (figure 1(d)) reveals a metallic behavior

with a gradual drop of resistance with decreasing temperature and with an increase below 20 K[1]. The fit of the low-temperature resistance data according to the 2D Mott variable range hopping model (top inset in figure 1(c)) gives $Ln(R) \sim T^{-1/3}$, suggesting that at low temperatures the carrier transport is dominated by localized states. This agrees with previous observations in FGT [8, 28]. The observation of a kink in resistance at $\sim$ 170 K, indicates a phase transition from a paramagnetic to a ferromagnetic state of FGT, as also shown clearly in the first derivative of resistance dR/dT (bottom inset of figure 1(c)). Such a transition agrees well with the Curie temperature (T_c) of FGT as reported recently [7, 23, 24].

2.2. AHE and magnetism in FGT

AHE measurements were performed in Hall-bar devices of FGT (20 nm) with Cr/Au contacts to characterize the magnetic properties of the samples. The presence of long-range magnetic order at low temperatures with PMA in the material allows the observation of a strong AHE signal (figure 1(e)). The AHE has been measured while sweeping the out-of-plane magnetic field and measuring transverse MR R_{xy}, which consists of ordinary and AHE components. The latter feature stems from intrinsic ferromagnetism in FGT. Since FGT is highly conductive with a high concentration of carriers, the ordinary Hall contribution is small compared to the anomalous signal within the measured field range, giving a flat magnetic field dependence after each switching.

To investigate the evolution of magnetism in FGT with temperature, we measured the AHE at different temperatures of 4–200 K (figure 2(a)). The Curie temperature (T_c) is obtained from AHE data using the Arrott plot analysis [14, 29] (figure 2(b)), where the R_{xy}^2 is plotted against B/R_{xy} at different temperatures. The intercept of the straight-line fittings, which changes from positive to negative when magnetic order transforms from ferromagnetic to paramagnetic state, is shown in the inset of figure 2(b). It crosses zero at 149.5 ± 8.0 K, which is the T_c in the measured FGT flake. It is less than reported for bulk samples of FGT with T_c of around 200 K [7, 30, 31]. Such a reduction of T_c is known to be present in thin flakes with a thickness below 20 nm [7, 8].

From the temperature dependence of the field sweeps, it is evident that the coercivity B_c decreases with temperature and disappears at $\sim$140 K, while the curve remains highly nonlinear (figure 1(c)). This suggests that magnetic order changes and magnetic domains are formed when the temperature approaches the Curie point. This transition persists up to about 170 K (figure 2(a)) when the R_{xy} dependence becomes linear. In the paramagnetic state, above the Curie temperature, the carrier sheet density and mobility were extracted by fitting the R_{xy} versus B data according to the ordinary Hall effect. To obtain the critical exponent, the temperature dependence of the anomalous Hall resistance $\Delta R_{xy,\text{sat}}$ can be fitted according to $\Delta R_{xy,\text{sat}} \sim (1 - T/T_c)^\beta$ [32]. The value of $\Delta R_{xy,\text{sat}}$ is the transverse resistance obtained after subtraction of the linear contribution from the ordinary Hall effect and is proportional to the
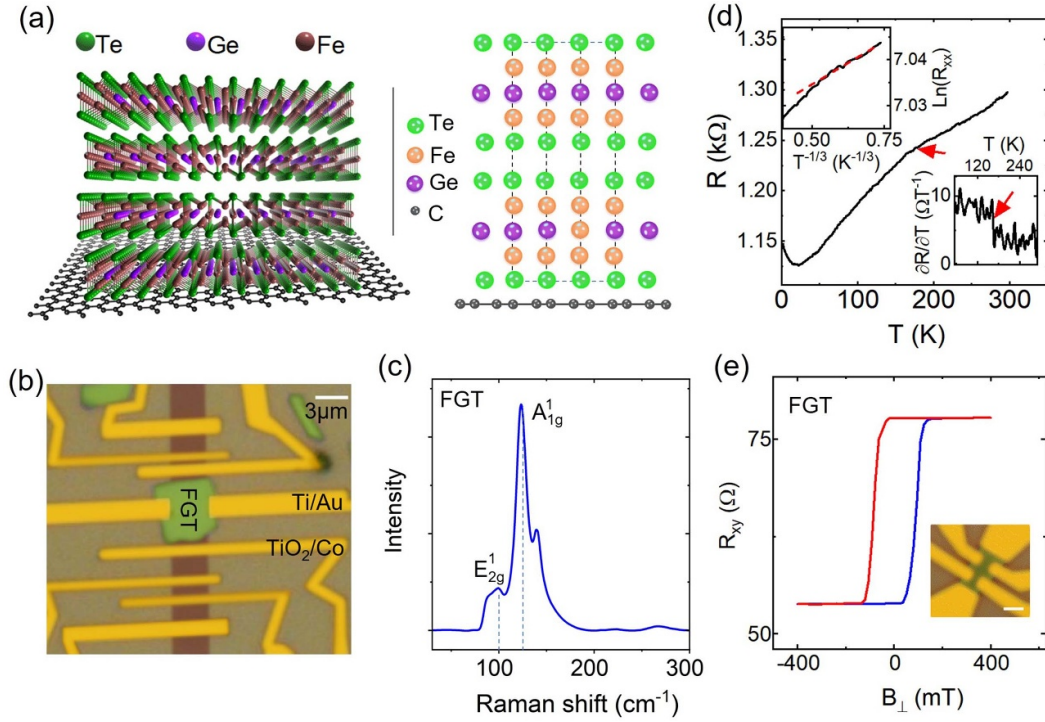
Figure 1. Graphene/FGT heterostructure and characterization of FGT. (a) Schematics of the graphene/FGT heterostructure. Right panel: atomic structure of interface of the graphene/FGT heterostructure. (b) Colored optical microscope picture of a representative device consisting of FGT flake on a CVD graphene (Gr) channel with non-magnetic Ti/Au contacts on FGT and graphene, and ferromagnetic tunnel contacts (Co/TiO$_2$) on graphene. The scale bar in the picture is 3 μm. (c) Raman spectrum of exfoliated FGT flake on SiO$_2$/Si substrate. (d) Temperature dependence of longitudinal two-terminal resistance of FGT. Insets are a fit according to the variable range hopping model (top left) and the first derivative of resistance dR/dT (bottom right). The red arrow indicates the T_c ~170 K for this FGT flake. (e) Transverse magneto resistance measured at 4 K in an FGT Hall bar device on SiO$_2$/Si substrate, as shown in a colored optical picture in the inset. The scale bar is 1 μm.

saturation magnetization of the FGT flake [31]. From the fitting (top panel in figure 2(c)), the value of $\beta = 0.34 \pm 0.06$ is obtained with T_c fixed at 150 K. This value of the critical exponent is characteristic of a 3D system (either Heisenberg, XY, or Ising model, which all have very close values of β) [32–34]. One could expect this for a flake thicker than 20 nm, as the dimensional crossover to a 2D system (consequently, reduction of β value) appears when T_c starts to drop with thickness, which occurs once the range of spin-spin interactions becomes larger than the sample thickness [35]. In FGT, the dimensional crossover has been reported for thicknesses below six monolayers [7, 31]. A similar dimensional crossover has been observed in Cr$_2$Gr2Te$_6$ with flakes less than six monolayers thick [9] and other magnetic thin films at few monolayer thicknesses [32, 35]. Considering the value of β one can conclude that T_c in the sample is determined by exchange interactions primarily, rather than by the excitation gap in 2D that results from magnetic anisotropy [9].

2.3. Angle dependence of AHE in FGT

To investigate the magnetic anisotropy of the FGT sample, the angle dependence of the AHE was measured. The MRs in the transverse R_{xy} (figure 2(d)) and longitudinal R_{xx} (figure 2(e)) directions were obtained while sweeping the magnetic field at

different angles from perpendicular to flake ($\psi = 0$) to in-plane directions. The angle dependence reveals the presence of sharp hysteresis loops in a perpendicular field direction. The coercive field B_c, increases as the angle is tilted towards the in-plane direction (figure 2(f)), while the amplitude of the MR jumps is reduced since it is caused only by the perpendicular component of the magnetic field. With a large enough in-plane field of about 2 T, the magnetic domains in FGT are forced in the in-plane direction. The observation of the AHE for the longitudinal MR is trivial and arises due to imperfections in the shape of the Hall bar, where side contacts used for measuring R_{xy} overlap with the channel. This allows for measurement of the transverse charge separation with Hall bar contacts on one side of the flake. Previously it has been shown that etching the flake into a perfect Hall bar shape can eliminate the AHE signal in R_{xx} [36]. Taking into account that the R_{xy} is proportional to the out-of-plane component of the magnetization M, the angle Θ between M and perpendicular direction was extracted as a function of ψ using equation $\Theta = \arccos(R_{xy,\psi}/R_{xy,\perp})$, where $R_{xy,\psi}$ is an amplitude of the transverse MR jump at an angle ψ and magnetic field of 500 mT (figure 2(g)). The Stoner–Wohlfarth model [37] was used to fit the data. According to the model, in equilibrium state the Zeeman energy E is minimal with respect to the magnetization angle Θ, giving rise to $K_u \sin(2\Theta) = M_s B \sin(\psi - \Theta)$. Here, M_s and K_u are the magnetic moment and magnetic anisotropic
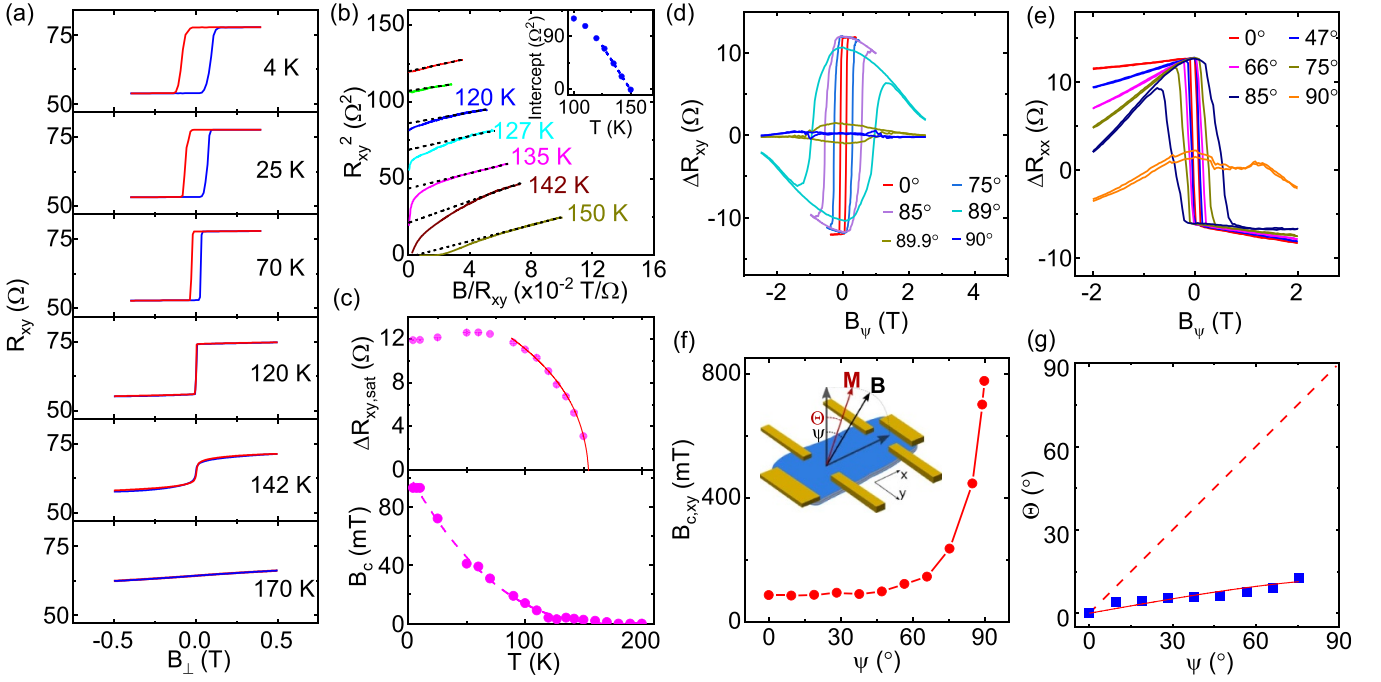
Figure 2. Temperature and angle dependence of the Anomalous Hall effect in FGT. (a) AHE data measured in the FGT Hall-bar device at different temperatures, as indicated. (b) Arrott plots of the AHE data. The inset shows the temperature dependence of the intercept. (c) Top panel: transverse resistance at saturation $\Delta R_{xy,\text{sat}}$, obtained after subtraction of the linear component. The red solid line is a fitting according to $\Delta R_{xy,\text{sat}} \sim (1 - T/T_c)^{\beta}$. Bottom panel: coercivity B_c as a function of temperature. The dashed line is a guide to the eye. (d), (e) AHE measured for transverse (R_{xy}) and longitudinal (R_{xx}) magnetoresistance at different angles at 4 K. (f) Coercivity as a function of angle ψ. Inset: schematics of the device configuration with noted angles between the out-of-plane direction and magnetization M (angle Θ) and magnetic field B (angle ψ). (g) Θ as a function of ψ (blue squares). The red dashed line represents the isotropic case $\Theta = \psi$, while the solid red line is a fitting according to the Stoner–Wohlfarth model.

energy per unit volume, respectively. Considering M_s to be 1.625 μ_B per atom of Fe [38] and FGT lattice constants [30] $a = b = 0.3953$ nm and $c = 1.6396$ nm, the fitting gives an estimation $K_u = 2.1 \times 10^5$ J m^{-3}. This value is similar to previous reports in FGT flakes of up to 10 nm in thickness [7, 31] and slightly above the value of $\sim 0.5 \times 10^5$ J m^{-3} reported in Cr$_2$Ge$_2$Te$_6$ [39]. Figure 2(g) shows that the magnetization angle changes with a delay with respect to the magnetic field direction. This confirms the strong perpendicular anisotropy of the FGT.

2.4. Graphene/FGT heterostructure characterization

Considering that the FGT vdW magnet has a metallic charge transport behavior and PMA, it is a potential candidate for a spin source on the graphene channel. We performed the electrical characterization of the FGT/graphene device to evaluate the vdW contact properties with temperature. The *I–V* characteristics (figure 3(a)) were measured in two-terminal configurations at different temperatures in the range of 4–300 K. The corresponding resistance versus bias voltage curves are shown in figure 3(b). Figure 3(c), shows the resistance with the temperature at 100 mV and 0 V. The vdW contact resistance increases from $R_i \sim 8.5$ kΩ at 300 K to $R_i \sim 12.5$ kΩ at 4 K at 100 mV bias voltage, where at zero bias the resistance

increases up to 18.5 kΩ at 4 K. Such a weak temperature dependence of the junction shows good quality of the FGT/Gr vdW interface over a wide range of temperatures.

To estimate the effect of FGT/Gr interface resistance on the expected MR in a spin valve device, we calculated the non-local spin resistance R_{nl} as a function of the contact resistance R_i using the spin diffusion model [40]. Figure 3(d) shows the calculation of the spin signal with FGT/Gr interface resistance, assuming different spin polarization of the FGT/Gr interfaces ($P \sim 10\%$–70%) and spin lifetime in our CVD graphene channel $\tau_s \sim 200$ ps and channel length of graphene ~ 2 μm. The calculated R_{nl} increases and saturates at an optimal R_i value. The dotted lines in the plot indicate the value of our measured FGT/graphene contact resistance range. Figure 3(e) show the calculation for two-terminal MR using model [41] with the same device parameters, which shows the possibility of observing a large MR in a narrow contact resistance R_i range. A small R_i gives rise to lower MR due to the conductivity mismatch preventing efficient spin injection from the FGT into graphene. The reduction of the MR for large R_i is due to the relaxation of the spins during the time spent in the graphene channel. Although spin injection and detection using FGT in graphene devices still need to be observed experimentally, the calculations provide information about the required device parameters and further optimization of FGT/graphene interfaces for efficient device operation.
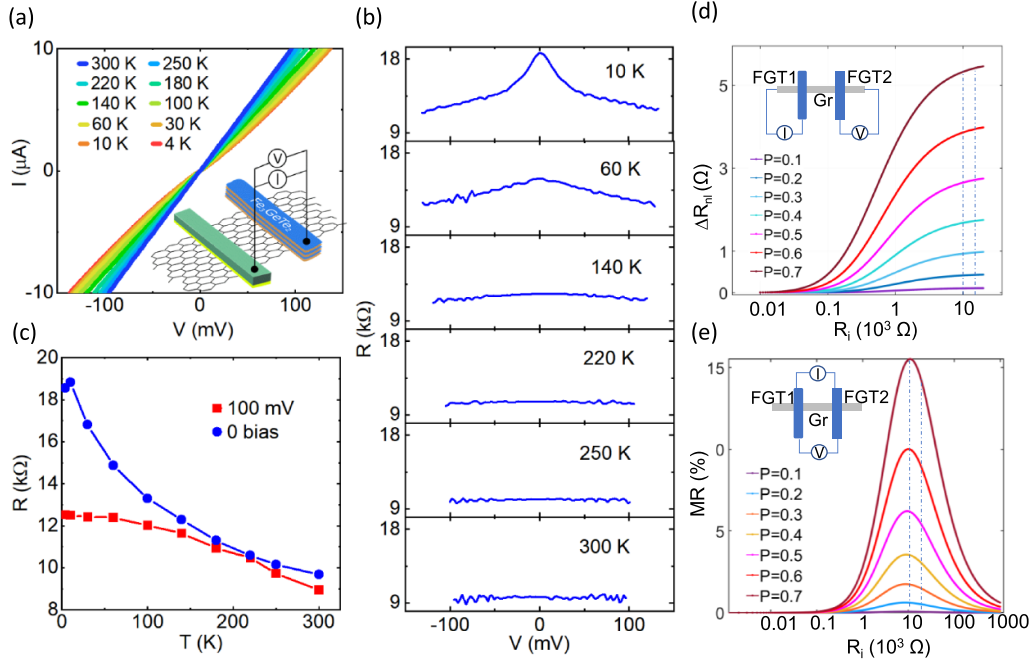
J. Phys. D: Appl. Phys. **56** (2023) 094001

B Zhao *et al*

Figure 3. Electrical characterization and magnetoresistance calculation for the graphene/FGT van der Waals heterostructure.
(a) Current–voltage characteristic of the graphene/FGT heterostructure with measurement geometry shown in the inset. (b) Differential resistance of graphene/FGT structure as a function of bias at different temperatures. (c) Temperature dependence of resistance at zero and 100 mV bias voltages. (d), (e) Calculated nonlocal and local spin valve signal magnitude as a function of the interface resistance (R_i) with different effective spin polarization of FGT. The *x*-axis is in a log scale.

2.5. Spin transport and absorption in graphene/FGT heterostructure

Next, we investigated spin transport and precession in FGT/Gr heterostructures employing spin valve and Hanle spin precession measurements using standard Co/TiO$_2$ ferromagnetic tunnel contacts for spin injection and detection on the CVD graphene channel. Our optimized CVD graphene devices are shown to be an excellent candidate for long distance spin transport and spin logic circuits [25, 42–45]. Figure 4(a) shows the device schematics of spin transport experiments in a nonlocal configuration in different channels, where channels with and without FGT are compared. We measured nonlocal spin valve voltage R_{nl} as a function of an external in-plane magnetic field ($B_{//}$) sweep (figure 4(b)) and Hanle spin precession signals R_{nl} are measured as a function of an out-of-plane magnetic field ($B_\perp$ sweep (figure 4(c)). It reveals that the spin signal amplitude ΔR_{norm} and spin lifetime τ_s are reduced when spin transport is measured in the heterostructure channel (ch3) in comparison to only graphene channels (ch1 and ch2), as shown in figure 4(d). To be noted, the spin signal amplitude ΔR_{norm} was calculated based on the nonlocal spin valve signal ΔR_{nl} extracted in Hanle signal (figure 4(c)) and normalized it to the same channel length of 3 μm. The estimated spin lifetimes τ_s are obtained from the fitting of the Hanle spin precession signals for the respective channels [46]. The presence of an FGT flake on the graphene can be viewed as a parallel transport channel. Thus, one of the possible scenarios is that

part of the spins accumulated in the heterostructure channel is absorbed by the FGT flake, leading to reduced spin transport parameters compared to pristine graphene channels. The efficiency of such absorption can also depend on the relative orientation between the spins in the channel and the direction of magnetization in FGT [47]. Furthermore, absence of hysteresis effect of the Hanle signal indicate that the magnetic proximity effect [12] in FGT/graphene interface is smaller than the detection limit and any stray field effect [48] can be ruled out.

To further elucidate the effect of FGT on spin absorption and spin relaxation in graphene channels, we calculate the spin absorption rate Γ using a simplified model [49, 50].

$$\Gamma = \frac{R_{gr} D_s}{\rho_{FGT} \lambda_{FGT} + R_i A} \approx \frac{R_{gr} D_s}{R_i A},$$

where R_{gr} and D_s are the graphene square resistance and spin diffusion constant, respectively. ρ_{FGT}, λ_{FGT} are the resistivity and spin diffusion length of FGT, respectively. R_i, A are the interface resistance and interface area of FGT/graphene heterostructure, where $\rho_{FGT} \lambda_{FGT}$ is ignorable compared to $R_i A$. Based on the experimental parameters of the CVD graphene devices, we can further calculate the spin lifetime from the spin absorption rate, i.e. $\tau_{s,abs} = 1/\Gamma$. Then the total spin relaxation time is given by $1/\tau_{s,tot} = 1/\tau_{s,SOC} + 1/\tau_{s,abs}$, where $\tau_{s,SOC}$ is the spin diffusion time of bare CVD graphene. One can find that the spin absorption contribution (figure 4(e)) ($R_{abs/tot} = \tau_{tot}/\tau_{abs}$) is around 10%–20% with FGT/Gr interface resistance 10–20 kΩ. As the calculation suggested, the

J. Phys. D: Appl. Phys. 56 (2023) 094001
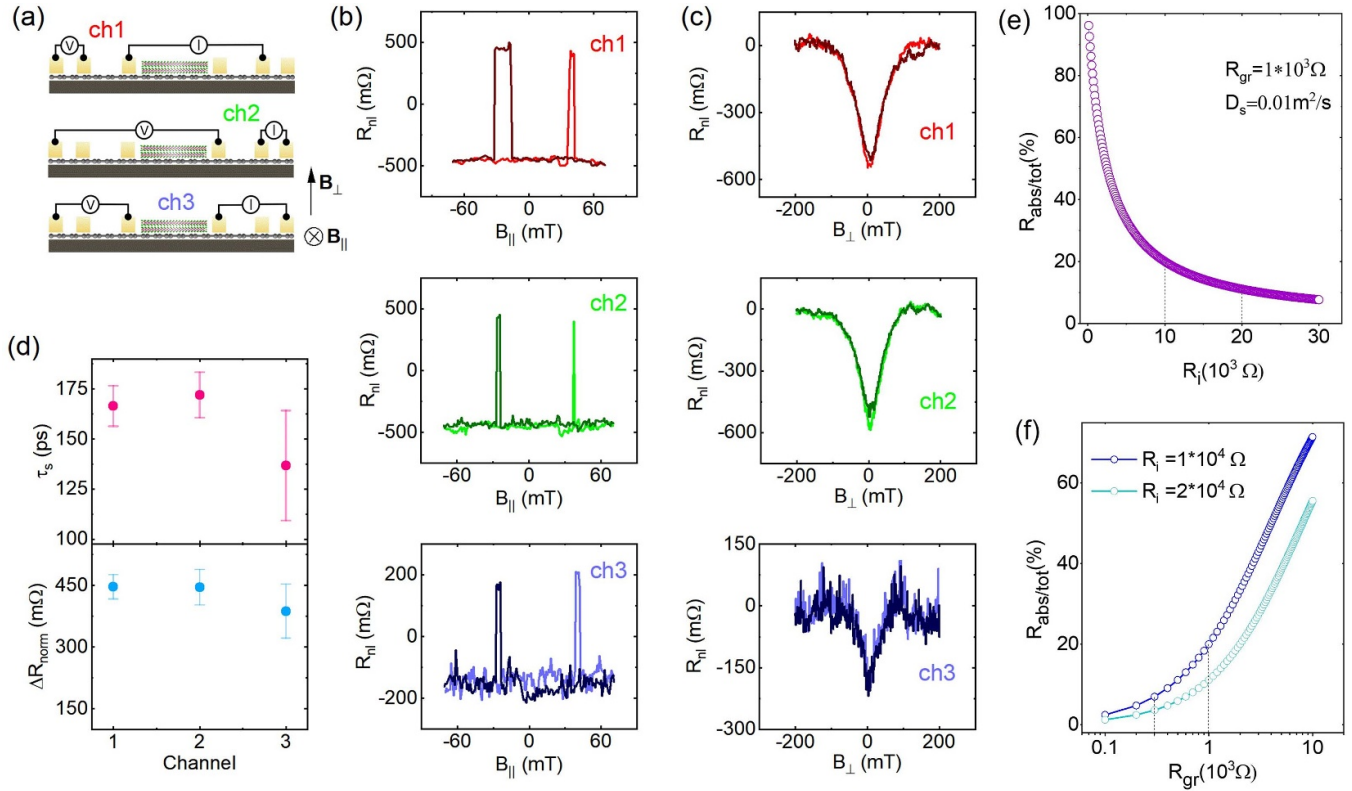
B Zhao *et al*

Figure 4. Spin transport in graphene/FGT heterostructure. (a) Schematics of the side view of the graphene/FGT device with Co/TiO$_2$ ferromagnetic tunnel contacts and nonlocal measurement schematics for three channels ch1 (3 μm), ch2 (3.3 μm), ch3 (4.5 μm), as indicated. Gr and FGT are indicated. (b), (c) The spin valve and Hanle measurements in the three channels ch1, ch2, and ch3, respectively measured at 50 K. (d) The spin lifetimes τ_s and normalized spin signal ΔR_{norm} with 3 μm channel length based on the fitting of the Hanle signals in (c). (e), (f) Calculated spin absorption ratio as a function of the interface resistance R_i and square resistance R_{gr} of the graphene channel, respectively. The dashed lines indicate the typical R_i and R_{gr} in our measuring devices.

spin absorption can be further tuned by different doping level-dependent-channel resistance (figure 4(f)).

3. Summary

FGT signifies an excellent vdW magnetic material with a strong out-of-plane magnetic anisotropy as observed from the detailed temperature and angle dependence measurement using AHE. The heterostructures of graphene with FGT exhibit tunneling transport behavior with a weak temperature dependence on the interface resistance. The spin transport properties of graphene in proximity to FGT indicate possible spin absorption and relaxation. The vdW nature of FGT opens opportunities for its utilization in heterostructures with graphene as a spin injector/detector and spin absorption or proximity-induced effects. These findings could be helpful for engineering vdW heterostructure devices and extend the opportunity for observation of possible new phenomena in condensed matter physics and device applications.

Data availability statement

The data that support the findings of this study are available from corresponding authors upon reasonable request.

ORCID iDs

Bing Zhao ⬤ https://orcid.org/0000-0002-5560-6750
Anamul Md Hoque ⬤ https://orcid.org/0000-0002-2117-7177
Saroj P Dash ⬤ https://orcid.org/0000-0001-7931-4843

References

[1] Klein D R *et al* 2018 Probing magnetism in 2D van der Waals crystalline insulators via electron tunneling *Science* **360** 1218–22

J. Phys. D: Appl. Phys. **56** (2023) 094001

B Zhao *et al*

[2] Song T *et al* 2018 Giant tunneling magnetoresistance in spin-filter van der Waals heterostructures *Science* **360** 1214–8

[3] Jiang S, Shan J and Mak K F 2018 Electric-field switching of two-dimensional van der Waals magnets *Nat. Mater.* **17** 406–10

[4] Burch K S, Mandrus D and Park J-G 2018 Magnetism in two-dimensional van der Waals materials *Nature* **563** 47–52

[5] Gong C and Zhang X 2019 Two-dimensional magnetic crystals and emergent heterostructure devices *Science* **363** eaav4450

[6] Gibertini M, Koperski M, Morpurgo A F and Novoselov K S 2019 Magnetic 2D materials and heterostructures *Nat. Nanotechnol.* **14** 408–19

[7] Deng Y *et al* 2018 Gate-tunable room-temperature ferromagnetism in two-dimensional Fe_3GeTe_2 *Nature* **563** 94–99

[8] Fei Z *et al* 2018 Two-dimensional itinerant ferromagnetism in atomically thin Fe_3GeTe_2 *Nat. Mater.* **17** 778–82

[9] Gong C *et al* 2017 Discovery of intrinsic ferromagnetism in two-dimensional van der Waals crystals *Nature* **546** 265–9

[10] Wilson N P *et al* 2021 Interlayer electronic coupling on demand in a 2D magnetic semiconductor *Nat. Mater.* **20** 1657–62

[11] Lee K, Dismukes A H, Telford E J, Wiscons R A, Wang J, Xu X, Nuckolls C, Dean C R, Roy X and Zhu X 2021 Magnetic order and symmetry in the 2D semiconductor CrSBr *Nano Lett.* **21** 3511–7

[12] Karpiak B *et al* 2019 Magnetic proximity in a van der Waals heterostructure of magnetic insulator and graphene *2D Mater.* **7** 015026

[13] Wang Z *et al* 2018 Electric-field control of magnetism in a few-layered van der Waals ferromagnetic semiconductor *Nat. Nanotechnol.* **13** 554–9

[14] Hu X, Zhao Y, Shen X, Krasheninnikov A V, Chen Z and Sun L 2020 Enhanced ferromagnetism and tunable magnetism in Fe_3GeTe_2 monolayer by strain engineering *ACS Appl. Mater. Interfaces* **12** 26367–73

[15] Wang Y *et al* 2020 Strain-sensitive magnetization reversal of a van der Waals magnet *Adv. Mater.* **32** 2004533

[16] Wang Z, Gutiérrez-Lezama I, Ubrig N, Kroner M, Gibertini M, Taniguchi T, Watanabe K, Imamoğlu A, Giannini E and Morpurgo A F 2018 Very large tunneling magnetoresistance in layered magnetic semiconductor CrI_3 *Nat. Commun.* **9** 2516

[17] Wang Z, Sapkota D, Taniguchi T, Watanabe K, Mandrus D and Morpurgo A F 2018 Tunneling spin valves based on Fe_3GeTe_2/hBN/Fe_3GeTe_2 van der Waals heterostructures *Nano Lett.* **18** 4303–8

[18] Ghazaryan D *et al* 2018 Magnon-assisted tunnelling in van der Waals heterostructures based on $CrBr_3$ *Nat. Electron.* **1** 344–9

[19] Zhong D *et al* 2017 Van der Waals engineering of ferromagnetic semiconductor heterostructures for spin and valleytronics *Sci. Adv.* **3** 1603113

[20] Alegria L D, Ji H, Yao N, Clarke J J, Cava R J and Petta J R 2014 Large anomalous Hall effect in ferromagnetic insulator-topological insulator heterostructures *Appl. Phys. Lett.* **105** 053512

[21] Wu Y *et al* 2020 Néel-type skyrmion in WTe_2/Fe_3GeTe_2 van der Waals heterostructure *Nat. Commun.* **11** 3860

[22] Zhao B, Ngaloy R, Hoque A M, Karpiak B, Khokhriakov D and Dash S P 2023 Room temperature spin-valve with van der Waals ferromagnet Fe_5GeTe_2/graphene heterostructure *Adv. Mater.* **35** 2209113

[23] Alghamdi M, Lohmann M, Li J, Jothi P R, Shao Q, Aldosary M, Su T, Fokwa B P T and Shi J 2019 Highly efficient spin-orbit torque and switching of layered ferromagnet Fe_3GeTe_2 *Nano Lett.* **19** 4400–5

[24] Wang X *et al* 2019 Current-driven magnetization switching in a van der Waals ferromagnet Fe_3GeTe_2 *Sci. Adv.* **5** eaaw8904

[25] Khokhriakov D, Sayed S, Hoque A M, Karpiak B, Zhao B, Datta S and Dash S P 2022 Multifunctional spin logic operations in graphene spin circuits *Phys. Rev. Appl.* **18** 064063

[26] Kong X, Berlijn T and Liang L 2021 Thickness and spin dependence of Raman modes in magnetic layered Fe_3GeTe_2 *Adv. Electron. Mater.* **7** 2001159

[27] Du L *et al* 2019 Lattice dynamics, phonon chirality, and spin–phonon coupling in 2D itinerant ferromagnet Fe_3GeTe_2 *Adv. Funct. Mater.* **29** 1904734

[28] Kim S-R, Park I K, Yoo J-G, Seo J, Kim J-G, Park J-H, Kim J S, Kim K, Lee G and Ko K-T 2022 Role of orbital bond and local magnetism in Fe_3GeTe_2 and Fe_4GeTe_2: implication for ultrathin nano devices *ACS Appl. Nano Mater.* **5** 10341–7

[29] Arrott A 1957 Criterion for ferromagnetism from observations of magnetic isotherms *Phys. Rev.* **108** 1394–6

[30] Deiseroth H, Aleksandrov K, Reiner C, Kienle L and Kremer R K 2006 Fe_3GeTe_2 and Ni_3GeTe_2—two new layered transition-metal compounds: crystal structures, HRTEM investigations, and magnetic and electrical properties *Eur. J. Inorg. Chem.* **2006** 1561–7

[31] Tan C, Lee J, Jung S-G, Park T, Albarakati S, Partridge J, Field M R, McCulloch D G, Wang L and Lee C 2018 Hard magnetic properties in nanoflake van der Waals Fe_3GeTe_2 *Nat. Commun.* **9** 1554

[32] Li Y and Baberschke K 1992 Dimensional crossover in ultrathin Ni(111) films on W(110) *Phys. Rev. Lett.* **68** 1208–11

[33] Li Z, Xia W, Su H, Yu Z, Fu Y, Chen L, Wang X, Yu N, Zou Z and Guo Y 2020 Magnetic critical behavior of the van der Waals Fe_5GeTe_2 crystal with near room temperature ferromagnetism *Sci. Rep.* **10** 15345

[34] Liu Y, Ivanovski V N and Petrovic C 2017 Critical behavior of the van der Waals bonded ferromagnet Fe_3GeTe_2 *Phys. Rev.* B **96** 144429

[35] Zhang R and Willis R F 2001 Thickness-dependent Curie temperatures of ultrathin magnetic films: effect of the range of spin-spin interactions *Phys. Rev. Lett.* **86** 2665–8

[36] Albarakati S *et al* 2019 Antisymmetric magnetoresistance in van der Waals Fe_3GeTe_2/graphite/Fe_3GeTe_2 trilayer heterostructures *Sci. Adv.* **5** eaaw0409

[37] Stoner E C and Wohlfarth E P 1991 A mechanism of magnetic hysteresis in heterogeneous alloys *IEEE Trans. Magn.* **27** 3475–518

[38] Chen B, Yang J, Wang H, Imai M, Ohta H, Michioka C, Yoshimura K and Fang M 2013 Magnetic properties of layered itinerant electron ferromagnet Fe_3GeTe_2 *J. Phys. Soc. Japan* **82** 124711

[39] Zeisner J, Alfonsov A, Selter S, Aswartham S, Ghimire M P, Richter M, van den Brink J, Büchner B and Kataev V 2019 Magnetic anisotropy and spin-polarized two-dimensional electron gas in the van der Waals ferromagnet $Cr_2Ge_2Te_6$ *Phys. Rev.* B **99** 165109

[40] Takahashi S and Maekawa S 2003 Spin injection and detection in magnetic nanostructures *Phys. Rev.* B **67** 052409

[41] Fert A and Jaffrès H 2001 Conditions for efficient spin injection from a ferromagnetic metal into a semiconductor *Phys. Rev.* B **64** 184420

[42] Kamalakar M V, Groenveld C, Dankert A and Dash S P 2015 Long distance spin communication in chemical vapour deposited graphene *Nat. Commun.* **6** 6766

J. Phys. D: Appl. Phys. **56** (2023) 094001

B Zhao *et al*

[43] Zhao B, Khokhriakov D, Karpiak B, Hoque A M, Xu L, Shen L, Feng Y P, Xu X, Jiang Y and Dash S P 2019 Electrically controlled spin-switch and evolution of Hanle spin precession in graphene *2D Mater.* **6** 035042

[44] Khokhriakov D, Karpiak B, Hoque A M and Dash S P 2020 Two-dimensional spintronic circuit architectures on large scale graphene *Carbon* **161** 892–9

[45] Khokhriakov D, Karpiak B, Hoque A M, Zhao B, Parui S and Dash S P 2020 Robust spin interconnect with isotropic spin dynamics in chemical vapor deposited graphene layers and boundaries *ACS Nano* **14** 15864–73

[46] Zhao B, Xu X, Wang L, Li J, Zhang Z, Liu P, Liu Q, Wang Z and Jiang Y 2018 Effect of Ti doping on spin injection and relaxation in few-layer graphene *Carbon* **127** 568–75

[47] Cosset-Chéneau M, Vila L, Zahnd G, Gusakova D, Pham V T, Grèzes C, Waintal X, Marty A, Jaffrès H and Attané J-P 2021 Measurement of the spin absorption anisotropy in lateral spin valves *Phys. Rev. Lett.* **126** 027201

[48] Karpiak B, Dankert A, Cummings A W, Power S R, Roche S and Dash S P 2017 1D ferromagnetic edge contacts to 2D graphene/h-BN heterostructures *2D Mater.* **5** 014001

[49] Khokhriakov D, Cummings A W, Song K, Vila M, Karpiak B, Dankert A, Roche S and Dash S P 2018 Tailoring emergent spin phenomena in Dirac material heterostructures *Sci. Adv.* **4** eaat9349

[50] Amamou W, Stecklein G, Koester S J, Crowell P A and Kawakami R K 2018 Spin absorption by *in situ* deposited nanoscale magnets on graphene spin valves *Phys. Rev. Appl.* **10** 044050